IJMMM International Journal of Minerals, Metallurgy and Materials 矿物冶金与材料学报（英文版）

Strengthening mechanisms of reduced activation ferritic/martensitic steels: A review

Jin-hua Zhou, Yong-feng Shen, and Nan Jia

Cite this article as:
Jin-hua Zhou, Yong-feng Shen, and Nan Jia, Strengthening mechanisms of reduced activation ferritic/martensitic steels: A review, *Int. J. Miner. Metall. Mater.*, 28(2021), No. 3, pp. 335-348. https://doi.org/10.1007/s12613-020-2121-1

View the article online at SpringerLink or IJMMM Webpage.

International Journal of Minerals, Metallurgy and Materials
Volume 28, Number 3, March 2021, Page 335
https://doi.org/10.1007/s12613-020-2121-1

Invited review

Strengthening mechanisms of reduced activation ferritic/martensitic steels: A review

Jin-hua Zhou[1)], *Yong-feng Shen*[2)], *and Nan Jia*[1)]

1) Key Laboratory for Anisotropy and Texture of Materials (Ministry of Education), School of Materials Science and Engineering, Northeastern University, Shenyang 110819, China
2) The State Key Lab of Rolling & Automation, Northeastern University, Shenyang 110819, China
(Received: 20 April 2020; revised: 11 June 2020; accepted: 17 June 2020)

Abstract: This review summarizes the strengthening mechanisms of reduced activation ferritic/martensitic (RAFM) steels. High-angle grain boundaries, subgrain boundaries, nano-sized $M_{23}C_6$, and MX carbide precipitates effectively hinder dislocation motion and increase high-temperature strength. $M_{23}C_6$ carbides are easily coarsened under high temperatures, thereby weakening their ability to block dislocations. Creep properties are improved through the reduction of $M_{23}C_6$ carbides. Thus, the loss of strength must be compensated by other strengthening mechanisms. This review also outlines the recent progress in the development of RAFM steels. Oxide dispersion-strengthened steels prevent $M_{23}C_6$ precipitation by reducing C content to increase creep life and introduce a high density of nano-sized oxide precipitates to offset the reduced strength. Severe plastic deformation methods can substantially refine subgrains and MX carbides in the steel. The thermal deformation strengthening of RAFM steels mainly relies on thermo-mechanical treatment to increase the MX carbide and subgrain boundaries. This procedure increases the creep life of TMT(thermo-mechanical treatment) 9Cr–1W–0.06Ta steel by ~20 times compared with those of F82H and Eurofer 97 steels under 550°C/260 MPa.

Keywords: reduced activation ferritic/martensitic steel; strengthening mechanism; high-angle grain boundary; subgrain boundary; precipitate

1. Introduction

Reduced activation ferritic/martensitic (RAFM) steels are promising cladding structure materials applied in nuclear fusion energy reactors because of their inherently superior thermal conductivity, relatively low thermal expansion, and resistance to radiation-induced swelling and helium embrittlement compared with austenitic stainless steels [1–3]. In the 1980s, ferritic stainless steels were mainly used as the cladding structure materials in nuclear fusion energy reactors. However, after long-term service, the steels show a relatively high radioactivity that is difficult to handle [4]. In 1984, Bloom *et al*. [5] first proposed the concept of low activation materials, and they believed that the radioactivity of the materials after irradiation mainly comes from the constituent highly active elements. Therefore, low activation elements such as V, Ta, Ti, and W should be selected rather than high activation elements such as Nb, Mo, Co, and Ni for the compositional design of cladding structure materials [6–7]. In 1989, Klueh *et al*. [8–10] first developed 9Cr2WVTa steel through a series of research on 2.25wt%–12wt% Cr steels. The tensile properties of the material are comparable to those of commercial 9Cr–1MoVNb heat-resistant steels. Since then, many countries have developed different types of RAFM steels, such as the F82H [11] and JLF series steels [12] in Japan, the EUROFER97 steel [13] in Europe, the China low activation martensitic (CLAM) steel [14] in China [12–13], the INRAFM steel in India [15], and the ARAA steel in South Korea [16]. So far, RAFM steels have achieved industrial production. For example, the F82H and EUROFER97 steels have reached the fabrication level of 10–20 t and the CLAM steel has reached the level of 6.5 t [17], respectively.

In the past 30 years, RAFM steels have achieved substantial progress, but many deficiencies remain. First, the poor long-term aging structure stability and the low high-temperature creep resistance of RAFM steels limit their service temperature and affect the conversion efficiency of the nuclear fusion reactor [2,18]. Second, the creep–fatigue cyclic softening phenomenon in RAFM steels limits the maximum

Corresponding authors: Yong-feng Shen E-mail: shenyf@smm.neu.edu.cn; Nan Jia E-mail: jian@atm.neu.edu.cn

load of the nuclear fusion reactor [19–20]. Third, the structure stability of RAFM steels is poor at high temperatures. The high temperature produced by welding leads to recrystallization and precipitate coarsening in the steels, reducing the high-temperature strength of the heat-affected zone and accelerating the joint creep damage in service at high temperatures and stresses [21–24]. Fourth, RAFM steels exhibit low impact performance after irradiation. Under irradiation conditions, the ductile brittle transition temperature (DBTT) of RAFM steels increases significantly, leading to high-temperature embrittlement and deteriorating safety performance [25–26]. Last, RAFM steels have poor dimensional stability. The steels encounter remarkable dimensional expansion when the irradiation dose exceeds 25 displacement per atom [27–28].

In recent years, a few studies have shown that nano-sized MX carbides significantly improve the high-temperature mechanical properties of RAFM steels. For example, oxide dispersion-strengthened (ODS) steels have remarkably better high-temperature mechanical properties than the traditional RAFM steels because the nano-sized oxide particles dispersed in ODS steels effectively block the dislocation motion during high-temperature creep [29–30]. Similarly, microalloying strengthening increases nanoparticle content because microalloying elements, such as V, Ti, and Ta, effectively promote MX carbide precipitation [31–33]. For example, Chen *et al*. [34] successfully increased the MX carbide content in low-carbon RAFM steels by adding Ta, thereby improving the creep rupture time under 550°C/180 MPa from 160 to 230 h.

Nevertheless, the high-temperature mechanical properties of RAFM steels do not always increase with increasing nano-sized MX carbides. Zhai *et al*. [35] suggested that nano-sized MX carbides can also increase significantly with the increase in Ta content in a RAFM steel with normal carbon content (0.1wt%), but the high-temperature mechanical properties decrease obviously. For example, the yield strength of RAFM steels decreases from 375 to 340 MPa at 700°C as the Ta content is increased from 0.03wt% to 0.15wt%. Our group also showed that Ti can effectively promote the precipitation of MX carbides in the CLAM steel. However, the high-temperature mechanical properties decrease with the addition of Ti because the formation of $M_{23}C_6$ carbides is inhibited by Ti alloying [36]. By contrast, Chen *et al*. [34] found that the amount of $M_{23}C_6$ carbides in a low-carbon RAFM steel is scarce because of the low-carbon content (<0.02wt%). The addition of microalloying elements only promotes the precipitation of MX. Therefore, the strengthening mechanism of RAFM steels is governed by other factors aside from the nano-sized precipitates because the high-temperature mechanical properties do not increase by merely adjusting a certain process to increase the formation of nano-sized MX carbides. Hence, the differences and connections of the various strengthening mechanisms in RAFM steels need to be discussed. This review summarizes the main strengthening mechanisms of RAFM steels and then presents the development of the steels in recent years.

2. Microstructure and strengthening mechanism

2.1. Microstructure

RAFM steels are the first option for fusion blanket structural materials because of their high service temperatures [37]. RAFM steels are usually martensitic, mainly consisting of prior austenitic grain boundaries, lath/sub grain boundaries, and precipitated phases, to meet the service demand at high temperatures [38]. Numerous laths and subgrain boundaries retain high strength at high temperatures by blocking dislocation motion. In general, precipitates in RAFM steels are classified as metastable and stable precipitates. The metastable ones mainly include M_3C, M_7C_3, and M_2X, and they exist only at low and medium temperatures but change to $M_{23}C_6$ and MX precipitates under high-temperature tempering [39]. Laves [40] and Z phases [41] may form in the steels after long exposure to elevated temperatures. Fig. 1 shows a schematic of the microstructure of a tempered RAFM steel. The RAFM steel consists of prior austenite grains with different orientations, and each grain contains several lath bundles with different orientations. Each lath bundle consists of several martensitic laths, and several $M_{23}C_6$ and MX carbides rest on the grain boundary, subgrain boundary, and matrix [42–43]. The number and character of grain boundaries, lath interfaces, and precipitates are closely associated with the macroscopic mechanical properties of the RAFM steel.

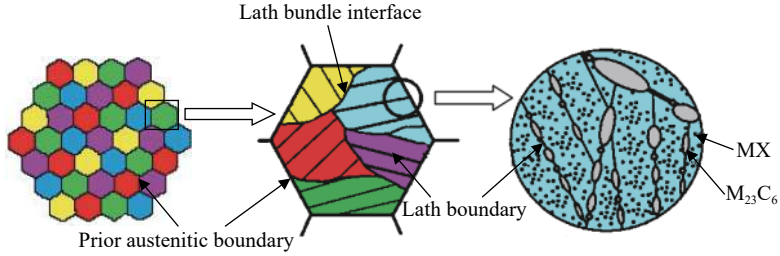

Fig. 1. Schematic of microstructures in the tempered RAFM steel.

2.2. Grain boundary strengthening

In general, the yield strength of metallic materials can be considerably improved by grain refinement [44]. The application of RAFM steels at high temperatures and low stresses requires high-temperature creep properties and good tensile properties. However, the influence of grain boundaries on the creep and tensile properties of polycrystalline materials is different. The creep process of polycrystals includes intragranular sliding and grain boundary sliding, which are closely related to temperature [45]. At low temperatures, a grain boundary can effectively block dislocation slip. Thus, the creep strength of materials increases with decreasing grain size, and the creep rate is positively proportional to the square of grain size (i.e., $\varepsilon \propto d^2$) [46]. At high temperatures, the binding force between the boundaries of neighboring grains is significantly weakened under shear stress, leading to grain boundary sliding [47], Fig. 2 is a schematic of grain boundary sliding during high-temperature creep. The creep strength of the material decreases with decreasing grain size, while the creep rate is inversely proportional to grain size (i.e., $\varepsilon \propto 1/d$) [48].

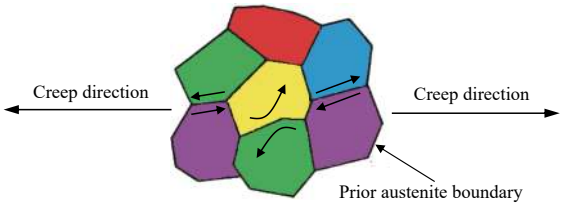

Fig. 2. Schematic of grain boundary sliding during high-temperature creep.

Grain boundaries exert harmful effects on high-temperature creep properties; thus, the microstructures of iron-based and nickel-based heat-resistant materials are usually designed as those with columnar crystals [49] or single crystal [50] to reduce the area of grain boundaries. Such a design improves high-temperature creep properties. Unfortunately, the service condition of RAFM steels is different from that of traditional heat-resistant materials. Apart from the high temperature, high irradiation is also a key factor. The defects caused by irradiation increase the microhardness of the material and lead to radiation hardening. The DBTT of the material increases with increasing irradiation dose [25–26]. When the DBTT value rises above room temperature, brittle fracture occurs with a large probability. In addition, grain size exerts a prominent effect on the DBTT value of metallic materials, and the relation between the DBTT value and grain size is expressed by the following equation [51]:

$$T_C = x - y \times d^{-1/2} \quad (1)$$

where T_C is the DBTT of a steel, x is a constant related to the chemical composition, y is the coefficient reflecting the ability of material to resist brittle crack propagation, and d is the grain size. Obviously, DBTT increases significantly with increasing grain size. Hence, a small grain size (i.e., 10–20 μm) is generally expected for RAFM steels [11–16].

2.3. Subgrain boundary strengthening

The misorientation of each martensitic lath in tempered martensite is unique. A small misorientation of ~2°–8° exists between adjacent martensitic laths [52]. Therefore, a single martensitic lath can be regarded as a "subgrain." In general, a subgrain boundary is a dislocation grid with a thickness of several atoms [53]. Thus, a subgrain can be considered as a small unit with different orientations separated by a dislocation wall [54]. Fig. 3 shows the morphology of subgrains and dislocation walls observed in a 304 stainless steel [55].

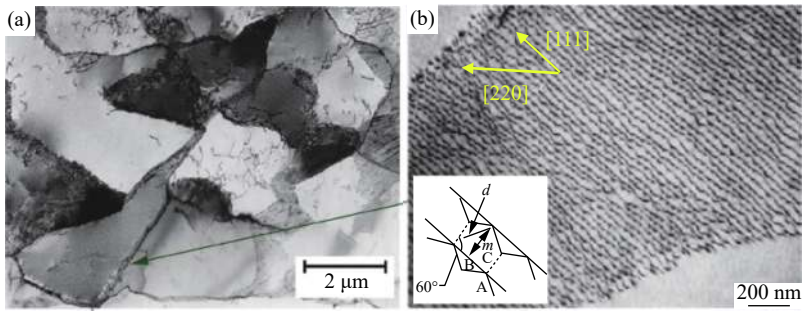

Fig. 3. Subgrains and dislocation wall observed by Kassner in a 304 stainless steel [55]. Reprinted from *Mater. Sci. Eng. A*, 410-411, M.E. Kassner, Recent developments in understanding the mechanism of five-power-law creep, 20, Copyright 2005, with permission from Elsevier.

Creep strength is related to dislocation density in the steel. At the beginning of creep, only a few dislocations appear in the steel [56], and the dislocation density increases greatly under external loading, following Frank–Read source mechanism [57] and double cross slip mechanism [58]. Consequently, the steel has a high initial instantaneous creep rate. With the subsequent progress of creep, dislocations interact with the precipitates and subgrain boundaries; hence, the dislocation motion is hindered, thereby decreasing the increasing speed of free dislocation density and creep rate [59]. In

addition, high temperatures lead to the recovery of dislocations and the reduction of dislocation density [60]. Indeed, subgrain boundaries consist of high-density dislocation walls. In addition, they may not slip as the high-angle grain boundaries during creep because of the minimal misorientation between subgrain boundaries. Therefore, subgrain boundaries can effectively block dislocation motion under the effect of external stress [61–62]. As creep proceeds, dislocations within the subgrains slip and then accumulate at the subgrain boundaries, leading to internal stress. As a result, the generation of dislocations is hindered, and internal stress continues to increase with the increase in dislocations at grain boundaries [63]. When the internal stress reaches the external stress, the internal stress on the grain scale reaches equilibrium and the dislocation proliferation stops. Thus, creep comes to a steady-state creep stage because the annihilation and generation of dislocation reach a balance and dislocation density remains identical [64]. A schematic of stress state at a subgrain boundary is shown in Fig. 4. The strength increment of the subgrain is calculated by using the following equation [65]:

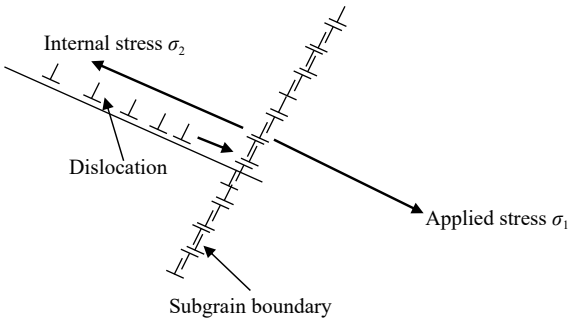

Fig. 4. Schematic of stress state at a subgrain boundary.

$$\Delta\sigma_{sgb} = MGb/\lambda \tag{2}$$

where M is the Taylor factor with a value of 3, G is the shear modulus (76 GPa for steel), b is the Burgers vector (2.85×10^{-10} m), and λ is the subgrain size. It shows that the creep strength of steels increases monotonically with decreasing subgrain size.

2.4. Precipitation strengthening

2.4.1. Effect of precipitate types

Precipitation strengthening is an important method in martensitic heat-resistant steels [66]. The dispersed fine precipitates effectively prevent the sliding of grain boundaries and dislocations at high temperatures, which significantly enhances the high-temperature strength of steels [67–68]. Tanaka *et al*. [69] suggested that the precipitation strengthening is maintained to a temperature of $0.65–0.7T_m$ (T_m is the temperature of melting point). The precipitates in RAFM steels are mainly $M_{23}C_6$ and MX carbides [39]. $M_{23}C_6$ carbides with a large diameter of 100–200 nm have a complex cubic lattice structure, and the lattice constant is 1.06–1.10 nm [70]. It is mainly distributed at the interface between austenite and martensitic lath, and can effectively block interface migration and dislocation slip [71]. The $M_{23}C_6$ precipitates and the matrix follow the relationship of $(011)_{M_{23}C_6}//(112)_{\alpha\text{-Fe}}$. The strengthening increment of $M_{23}C_6$ carbides is evaluated by using the dispersed barrier hardening (DBH) model [72]:

$$\Delta\sigma_{M_{23}C_6} = M\alpha Gb\sqrt{Nd} \tag{3}$$

where M is the Taylor factor with a value of 3, G is the shear modulus (76 GPa for steel), α is the barrier strength factor (1.0 for voids), N is the density, and d is the average size of $M_{23}C_6$ carbides, respectively.

The size of MX-type carbonitride is relatively small (<30 nm). It has a face-centered cubic (fcc) lattice structure, and the lattice constant is 0.41–0.45 nm [73]. The MX precipitates and the matrix follow a relationship of $(011)_{MX}//(111)_{\alpha\text{-Fe}}$. They are mainly distributed in the martensitic lath and play an important role in hindering dislocation slip [69]. The strengthening increment of MX carbides can be calculated by using the Orowan strengthening mechanism [74]:

$$\Delta\sigma_{MX} = \frac{0.7MGb\sqrt{f_v}}{d} \tag{4}$$

where f_V is the volume fraction of precipitates and d is the average size of precipitates.

Considering that the main forming element of $M_{23}C_6$ and MX carbides is carbon, we carry out a comparative calculation on the strengthening of two types of precipitates formed by the same number of carbon atoms in unit volume:

$$\frac{\Delta\sigma_{M_{23}C_6}}{\Delta\sigma_{MX}} = \frac{M\alpha Gb\sqrt{N_{M_{23}C_6}d_{M_{23}C_6}}}{\dfrac{0.7MGb\sqrt{f_{vMX}}}{d_{MX}}} = \frac{\sqrt{2N_{M_{23}C_6}r_{M_{23}C_6}}}{\dfrac{0.7\sqrt{4/3N_{MX}\pi r_{MX}^3}}{2r_{MX}}} = \frac{\sqrt{2N_{M_{23}C_6}r_{M_{23}C_6}}}{\sqrt{0.51N_{MX}r_{MX}}} \tag{5}$$

where r is the average radius of $M_{23}C_6$ carbides. The radius of $M_{23}C_6$ carbides is about three times that of MX carbides because the number of C atoms in the two precipitates is identical ($N_{M_{23}C_6} = 6N_{MX}$). Thus, we obtain $\Delta\sigma_{M_{23}C_6}/\Delta\sigma_{MX} = 1.4$. That is, the strengthening effect of $M_{23}C_6$ carbides is 1.4 times higher than that of MX carbide, provided with the same amount of C atoms. The calculated result is consistent with the findings of our group [36]. However, our study shows that the large $M_{23}C_6$ particles promote dislocation accumulation and consequently induce stress concentration. This phenomenon undoubtedly results in crack initiation and propagation, reducing the plasticity of steels [36].

2.4.2. Thermal stability of precipitates

At high temperatures, $M_{23}C_6$ and MX carbides become coarse. The coarsening mechanism of the two precipitates conforms to Oswald ripening, i.e., small particles dissolve

and large particles coarsen [75–76]. Oswald ripening significantly decreases the amount of precipitates and increases the size of precipitates, reducing the strengthening effect of the precipitates (Eqs. (4) and (5)). However, the thermal stability of $M_{23}C_6$ and MX carbides is different. RAFM steels are usually applied in an environment of 500–600°C. The dissolution temperature of $M_{23}C_6$ carbides is ~830°C, indicating that they are easy to coarsen under the service condition [77–78]. By contrast, the dissolution temperature of MX carbides is >1200°C, which has good thermal stability under the service condition of steels [79–80]. Sawada *et al*. [81] reported that the coarsening rate of MX carbides is only 1/10 that of $M_{23}C_6$ carbides at 500–600°C. Therefore, despite the high contribution of $M_{23}C_6$ carbides to strength, its low thermal stability makes the strengthening effect of the steel at high temperatures very limited [82–83]. Hence, the contents of two types of precipitates in steels must be controlled to retain a good combination of thermal stability and creep strength.

2.4.3. Radiation resistance of nanoprecipitates

The radiation damage of RAFM steels in a fusion reactor is mainly caused by the collision of neutrons and crystal atoms [84]. Once the collided atoms obtain enough energy, they overcome the restriction of surrounding atoms and move from the original position. As a result, the atom is called a gap atom, which leaves a vacancy at the previous lattice point to form a Frank defect. Provided with more energy, the collided atoms must collide with other atoms when they leave the initial lattice point. This process leads to the formation of a series of Frank defects. The shift atoms produced by the initial collision of incident neutrons and lattice atoms are called primary knock-on atoms [85], whereas the subsequent collisions caused by the displaced atoms are called cascade collisions [86]. The formation of dislocated atoms and vacancies leads to the irradiation swelling of steels. Hence, the dimension of the material increases and the toughness significantly decreases.

Nano-sized MX carbides greatly reduce the irradiation vacancy content in steels. The main reason is that the nucleation energy of the vacancy at the interface is much lower than that at the matrix. Meanwhile, the nano-sized MX carbides significantly increase the interface area within steels, which makes the vacancy easy to nucleate at the interface between the MX carbides and the matrix but difficult to migrate and aggregate [87–88]. In addition, the MX carbides completely precipitate in the solution treatment stage of a steel because of the high precipitation temperature, allowing effective grain refinement [89]. Consequently, the increasing grain and subgrain boundary area significantly hinders the movement and aggregation of dislocations, leading to local hardening [90]. Fig. 5 is a schematic of dislocation motion and vacancy migration in a steel without precipitates compared with that containing the MX carbides after irradiation.

2.5. Comparison of different strengthening mechanisms

Fig. 6 shows the typical high-temperature creep curve of a RAFM steel. The creep process can be divided into three stages, i.e., initial creep stage (Ⅰ), steady-state creep stage (Ⅱ), and accelerated creep stage (Ⅲ) [91]. The initial creep stage usually shows a fast creep rate due to the low free dislocation density. As the dislocation density increases, the creep gradually progresses into the steady-state creep stage (see Section 2.3 in detail). The steady-state creep stage is the most important of the three, and the creep rate at this stage remains

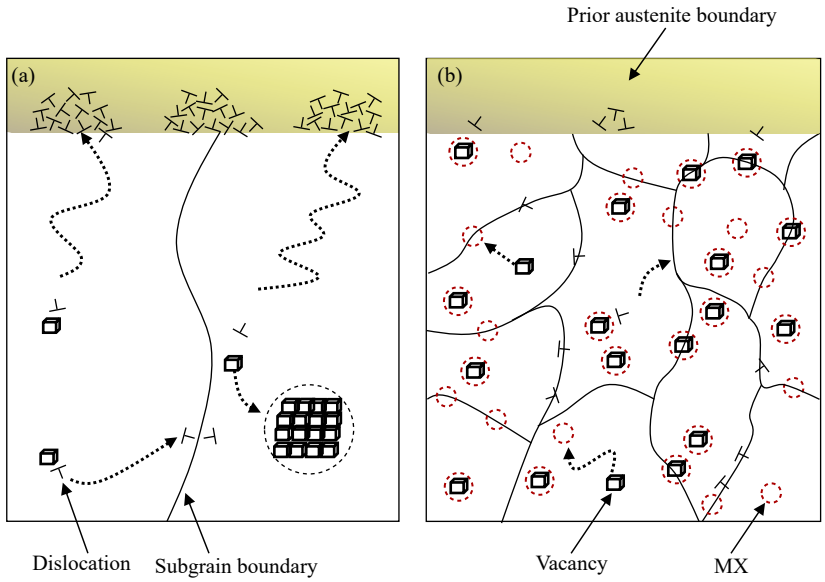

Fig. 5. Schematic of dislocation motion and vacancy migration in the steel during irradiation: (a) without MX carbides; (b) with MX carbides.

constant ($\Delta\varepsilon/\Delta T$ is constant). The creep rate reflects the resistance ability of the microstructure to dislocation motion, and the duration of steady-state creep stage is mainly determined by the high-temperature structure stability of steels [47]. At high temperature and/or applied stress, the sub-crystals and precipitates become coarse. Meanwhile, grain boundary sliding greatly reduces the ability of blocking dislocations. Therefore, the creep rate increases and reaches the accelerated creep stage. The increasing high-angle grain boundaries (HAGBs), subgrain boundaries, and nano-sized MX carbides improve the high-temperature strength and microstructure stability of the steels. Although $M_{23}C_6$ carbides effectively improve high-temperature strength, their poor high-temperature stability greatly reduces creep life and their large size deteriorates ductility. Therefore, at present, the improvement of creep properties is mainly achieved by reducing the $M_{23}C_6$ carbide content to increase the high-temperature structure stability of steels through other strengthening mechanisms that offset the strength reduction. The research of new RAFM steels is still in infancy, and systematic research on radiation damage mechanism has not been reported. Therefore, the following sections only discuss the microstructures and mechanical properties of new RAFM steels without irradiation.

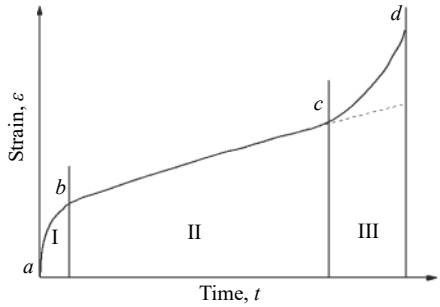

Fig. 6. Typical high-temperature creep curve of the RAFM steel.

3. Recent development of RAFM steels

3.1. Oxide dispersion-strengthened (ODS) steel

The main design idea of ODS steels is to greatly reduce the C content for inhibiting the precipitation of $M_{23}C_6$ carbides and concurrently introduce numerous nanoscale oxide precipitates for offsetting the strength reduction caused by the reduction of $M_{23}C_6$ carbides. Oxides have better thermal stability because of their higher dissolution temperature than $M_{23}C_6$ and MX carbides [92]. Thus, the induced nanoscale oxide particles improve the precipitation strengthening and thermal stability of steels simultaneously. In the 1960s, SCK CEN in Belgium developed the first ODS steel [93]. At first, Y_2O_3 is the main oxide in ODS steel because Y_2O_3 particles have strong anti-radiation decomposition and anti-oxidation peeling abilities [94]. However, the size of Y_2O_3 in ODS steels is usually large (~30–40 nm), leading to the limited strengthening effect. Klueh *et al*. [95] reported that adding Ti to the ODS steel results in the formation of fine Y–Ti–O particles with a size of 3–5 nm. By contrast, the size of MX carbides in the EUROFER97 steel is 20–30 nm [96]. Subsequently, Al was introduced to improve the corrosion resistance of ODS steels. Given the strong oxygen affinity of Al, Y–Al–O particles are preferentially precipitated in Ti-containing ODS steels. However, the large Y–Al–O particles (~10–20 nm) cause the significant reduction of mechanical properties of the steel compared with the fine Y–Ti–O precipitates [97]. To overcome this problem, Dou *et al*. [98] refined the oxide particles to 7 nm by adding Zr in an Al-containing ODS steel. Yan further refined the oxide particles to 4 nm by adding Hf in an Al-containing ODS steel [99]. As a result, the high-temperature strength and radiation resistance of the ODS steel are much higher than those of the RAFM steel in the same period. Fig. 7 shows a comparison of the high-temperature creep performance and radiation resistance between ODS and RAFM steels in recent years [100–103]. The creep life of the 9Cr ODS steel is ~1000 times longer than that of the F82H and Eurofer 97 steels under 650°C/130 MPa. Thus, the ODS steel is a possible candidate to meet the service requirements of next-generation nuclear fusion reactors.

Nevertheless, the preparation process of ODS steels is complex. Thus, the fabrication is difficult to be industrialized at present. ODS steels are mainly prepared via powder metallurgy [104], and a schematic of the preparation process is shown in Fig. 8. In brief, the metal and oxide particles are separately milled to nanometer powders, and then the metallic and oxide powders are mixed by mechanical alloying to promote the homogeneity of the material. The mechanical alloying powders are sintered via hot isostatic pressing to enhance the compactness of the material and promote the nucleation of nano-sized oxide particles in steels. Finally, the microstructure of the steel is further controlled by deformation processing and heat treatment. Ball milling and mechanical alloying are difficult to control. Thus, they may lead to the discrepancy of chemical compositions of ODS steels. Moreover, the preparation process is complex, time consuming, and inefficient, leading to a great increase in the production cost of ODS steels [105]. At present, the development of ODS steels is mainly focused on how to improve production capacity and efficiency to achieve mass production of bulk ODS steels.

3.2. Machining strengthened RAFM steel

Machining strengthening can be divided into cold deformation and thermal deformation. The main idea of the cold deformation strengthening of RAFM steels is to greatly refine subgrains and carbides by introducing severe plastic deformation (SPD) [106–107] at low temperatures in order to increase subgrain boundary strengthening and precipitation

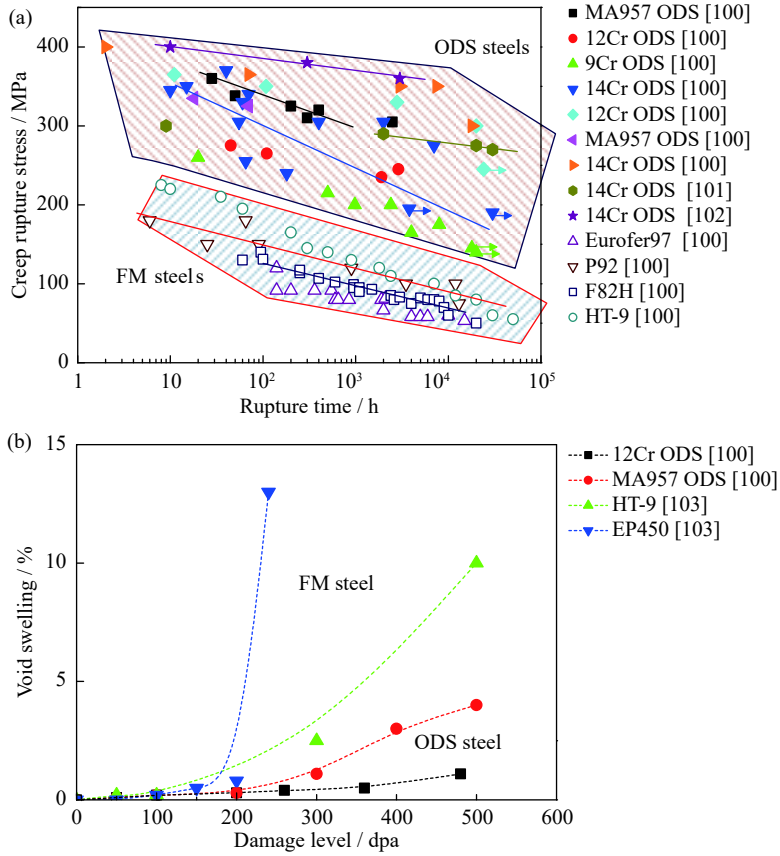

Fig. 7. Comparison of high-temperature creep strength at 650°C (a) and irradiation resistance at 450–480°C (b) between ODS and RAFM steels in recent years.

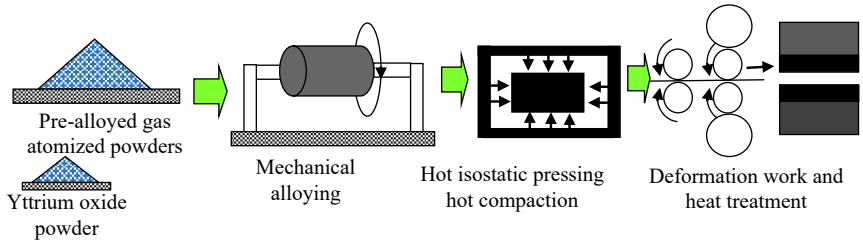

Fig. 8. Schematic of the preparation processes of ODS steels [104]. Reprinted from *J. Nucl. Mater.*, 518, T. Jaumier, S. Vincent, L. Vincent, and R. Desmorat, Creep and damage anisotropies of 9%Cr and 14% Cr ODS steel cladding, 274, Copyright 2019, with permission from Elsevier.

strengthening. In 2011, Wang *et al.* [108] first prepared ultrafine subgrained P91 steel through surface mechanical attrition treatment (SMAT). They successfully reduced the average diameter of subgrains and $M_{23}C_6$ carbides to 35 and 20 nm, respectively, from 320 and 125 nm in the traditional RAFM steel, respectively. However, SMAT is a SPD method to synthesize the nanostructured surface layer on metallic materials; thus, it cannot fabricate samples with large dimensions. Later, Chen *et al.* [109] prepared an ultrafine subgrained RAFM steel by cold forging and post-annealing, which reduced the subgrain and $M_{23}C_6$ carbide size to 240 and 60 nm, respectively. Compared with the traditional quenching plus tempering process, cold forging and post-annealing successfully increase the yield strength of the RAFM steel from 550 to 650 MPa and elongation from 18% to 25%. Recently, Jin *et al.* [110] have prepared an ultrafine subgrained 9Cr2WVTa steel by multi-pass rotary-swaging and post-annealing, and reduced the subgrain and $M_{23}C_6$ carbide sizes to 330 and 50 nm, respectively. The creep life of ultrafine grained 9Cr2WVTa steel at 550°C has been greatly improved, i.e., 550 h at an applied stress of 270 MPa and exceeding 1300 h at an applied stress of 250 MPa. By contrast, the creep lives of the Eurofer 97 and F82H steels are merely 17, 50, and 150 h under identical creep conditions. The creep life of the cold deformed 9Cr2WVTa steel is 30 times higher than that of the F82H and Eurofer 97 steels under 550°C/270

MPa. The comparison of creep lives among ultrafine subgrained 9Cr2WVTa, typical Eurofer 97, and F82H steels is shown in Fig. 9.

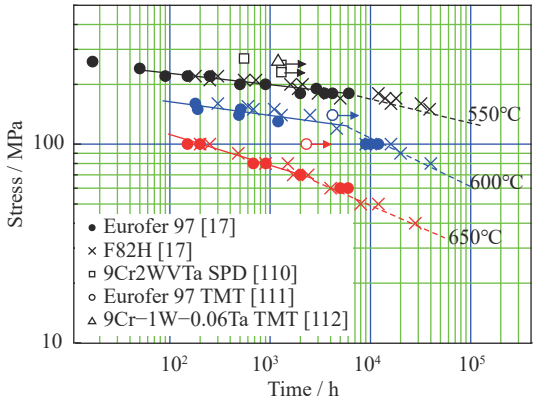

Fig. 9. Creep properties of cold deformation and thermal deformation-strengthened steels compared with typical Eurofer 97and F82H steels.

The thermal deformation of RAFM steels is mainly associated with thermo-mechanical treatment (TMT) [113]. The main idea of TMT is to reduce the $M_{23}C_6$ carbide precipitation strengthening and replace it with MX carbide precipitation strengthening, grain boundary strengthening, and subgrain boundary strengthening. The goal is to increase thermal stability and improve the high-temperature creep properties without losing the strength of steels. Fig. 10 shows a schematic of the structural change in a steel under TMT processing. First, the steel is heated above the austenitizing temperature (1050–1300°C) to dissolve the precipitate and then cooled to 700–1000°C for hot rolling. These procedures introduce high-density dislocations and reduce subgrains. Meanwhile, the precipitation of MX carbides instead of $M_{23}C_6$ carbides is promoted. Finally, the steel is annealed at 650–800°C to obtain completely recrystallized grains and completely precipitate $M_{23}C_6$ carbides [114]. In 2016, Hoffmann *et al.* [111] treated the Eurofer 97 steel by using TMT at a thermal deformation temperature of 700°C and annealing temperature of 750°C. TMT significantly improves the high-temperature creep properties of the Eurofer 97 steel to >2300 h at 650°C/100 MPa and >4200 h at 600°C/140 MPa. By contrast, the creep lives of the typical Eurofer 97 and F82H steels at identical creep conditions are about 1000 and 200 h, respectively. So far, no systematic analysis is conducted on the microstructural change before and after TMT. Prakash *et al.* [115] prepared a 9Cr–1W–0.06Ta RAFM steel via TMT at a thermal deformation temperature of 700°C and annealing temperature of 760°C. Compared with traditional quenching plus tempering, prior austenitic grain size significantly increases from (10 ± 2) μm to (175 ± 12) μm, the $M_{23}C_6$ carbide size decreases from 50–150 nm to 30–100 nm, the MX carbide size decreases from 20–50 nm to 5–30 nm, and the subgrain size decreases from 272 nm to 179 nm [110]. As expected, the high-temperature creep life of the steel significantly increases to 1200 h at 550°C/260 MPa [112] compared with ~50 h under the same creep conditions for typical Eurofer 97 and F82H steels [17]. The creep life of the TMT-processed 9Cr–1W–0.06Ta is about 20 times higher than that of the F82H and Eurofer 97 steels under 550°C/260 MPa. Comparison of the creep lives between two types of TMT steels and the typical Eurofer 97 and F82H steels is summarized in Fig. 9.

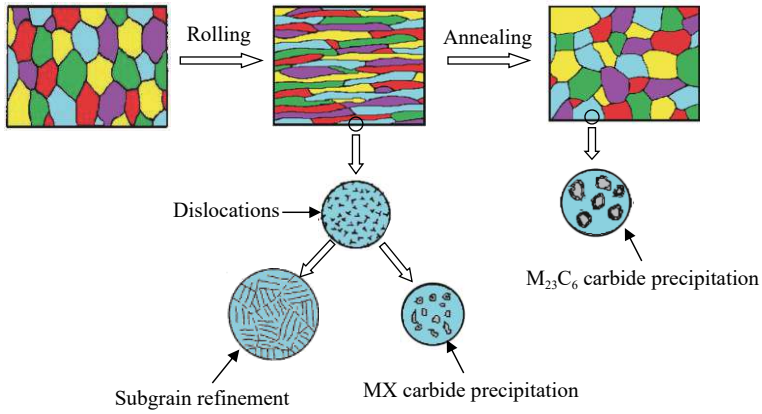

Fig. 10. Schematic of the microstructural variation in RAFM steel under thermo-mechanical treatment (TMT).

3.3. Microalloying and unconventional heat treatment strengthening

Microalloying elements, such as Ti, Mo, V, and Ta, are strong carbide-forming elements. In steels, these elements easily form stable MX carbides [33]. Theoretically, the addition of microalloying elements can significantly promote the precipitation of MX carbides and inhibit the precipitation of $M_{23}C_6$ carbides because the precipitation temperature of the former is considerably higher than that of the latter [77–78]. For example, Xiao *et al.* [112,116] suggested that adding V

and Ta in RAFM steels not only leads to the precipitation of MX carbides but also refines $M_{23}C_6$ carbides. Basing from this idea, we prepared a CLAM steel containing 0.10wt% Ti by controlling the tempering and other preparation processes. Strength reduction caused by the decreasing $M_{23}C_6$ is compensated by increasing the subgrain strengthening [117]. Table 1 shows the microstructure information of 0.10wt% Ti CLAM steels treated with different tempering processes [117], and the conventional CLAM steel without Ti is included for comparison. Due to the same rolling and quenching process, the grain size and MX carbide size of the steels show insignificant variations, i.e., 7 and 17 nm, respectively. With the decrease in tempering temperature and time, the sizes of the subgrains and $M_{23}C_6$ carbides decrease significantly. To be explicit, they are 650 and 90 nm, 450 and 60 nm, and 370 and 40 nm, after tempering processing at 760°C/90 min, 760°C/30 min, and 730°C/30 min, respectively. The corresponding densities of the $M_{23}C_6$ carbides are 2.85×10^{19}, 4.30×10^{19}, and 1.10×10^{20} m^{-3}, respectively. Compared with those in the conventional CLAM steels, the sizes of grains and densities of $M_{23}C_6$ and MX carbides decrease, whereas the sizes of subgrains and densities of $M_{23}C_6$ and MX increase in 0.10wt% Ti CLAM steels after tempering at 760°C/90 min. With decreasing tempering temperature and time, the sizes of subgrains and $M_{23}C_6$ carbides continuously decrease and the densities of $M_{23}C_6$ carbides increases. The above-mentioned strengthening mechanism (Section 2) indicates that Ti addition promotes MX precipitate strengthening but restrains the strengthening from subgrain boundaries, grain boundaries, and $M_{23}C_6$ precipitates.

Table 1. Microstructure information of 0.10wt% Ti CLAM steel fabricated via different tempering processes compared with their counterparts without Ti addition

Steel	Grain size / nm	Subgrain / nm	$M_{23}C_6$		MX	
			Size / nm	Density / m^{-3}	Size / nm	Density / m^{-3}
0.1 Ti CLAM (760°C/90 min)	7	650	90	2.85×10^{19}	17	8.20×10^{24}
0.1 Ti CLAM (760°C/30 min)	7	450	60	4.30×10^{19}	17	8.20×10^{24}
0.1 Ti CLAM (730°C/30 min)	7	370	40	1.10×10^{20}	17	8.20×10^{24}
CLAM [114]	20	320	125	6.05×10^{19}	30	3.20×10^{24}

The microstructural change related to Ti addition and tempering is due to the fact that Ti effectively promotes the nucleation of MX carbides, whereas the dispersed fine MX particles refine grains by hindering grain growth at the solid solution stage in martensitic steels. In consideration that the melting point of $M_{23}C_6$ is remarkably lower than that of MX carbides, the formation of $M_{23}C_6$ carbides is inhibited. The small $M_{23}C_6$ carbides induce the increment of martensite lath size by hindering the growth of martensite lath during tempering. The tempering processes are 760°C/90 min, 760°C/30 min, and 730°C/30 min, respectively, and those temperatures are close to the precipitation temperature of $M_{23}C_6$ carbides. Therefore, the size of $M_{23}C_6$ carbides decreases significantly with decreasing tempering temperature and time. The different tempering processes show insignificant effect on MX carbides because the precipitation temperature of the carbides is high. In addition, the austenitizing temperature of 805°C [117] is above the tempering temperature. Hence, the size of the primary austenitic grains remains constant despite the slightly decreasing subgrain size with reduced temperature and time for tempering.

Fig. 11 shows the engineering stress–strain plots of 0.10wt% Ti CLAM steels with different tempering processes at 600°C compared with the standard CLAM steel [117]. The tensile strength (σ_{TS}) and yield strength (σ_y) of the 0.10wt% Ti CLAM steel treated by 760°C/90 min tempering are 285 and 260 MPa, respectively, and the maximum elongation is 47%. With the decrease in tempering temperature and time, σ_{TS} and σ_y increase while elongation decreases, which are respectively 340 MPa, 325 MPa, and 33% at 760°C/30 min and 370 MPa, 345 MPa, and 29% at 730°C/30 min. For the conventional CLAM steel, the σ_{TS}, σ_y, and elongation are 305 MPa, 325 MPa, and 27%, respectively. Except for the 0.10wt% Ti CLAM steel tempered at 760°C/90 min, the σ_{TS}, σ_y, and elongation of the 0.10wt% Ti CLAM steel are higher than those of the conventional CLAM steel. Fig. 12 shows the creep curves of the 0.10wt% Ti CLAM steels fabricated

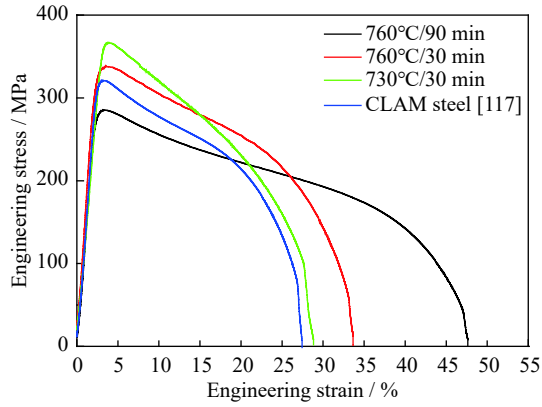

Fig. 11. Engineering stress–strain plots for the 0.10wt% Ti CLAM steels via different tempering processing at 600°C. The stress–strain curve for the steel without Ti addition is also shown for comparison.

by different tempering processes. Creep experiments were conducted at 600°C/170 MPa. At this condition, the creep life and elongation of the 0.10wt% Ti CLAM steels tempered at 760°C for 90 min are 20 h and 50%, respectively. The creep life of the 0.10wt% Ti CLAM steel increases and its creep elongation decreases with decreasing tempering temperature and time, reaching 145 h and 30% at 760°C/30 min and 190 h and 25% at 730°C/30 min. The creep life and ductility are significantly higher than 120 h and 20% for the conventional CLAM steel, respectively [118]. Obviously, adding Ti and adjusting the tempering process increases the high-temperature creep life of the CLAM steel successfully without sacrificing the ductility. The processing of the Ti CLAM steel is simple compared with that of the traditional CLAM steel, which is beneficial to commercial production.

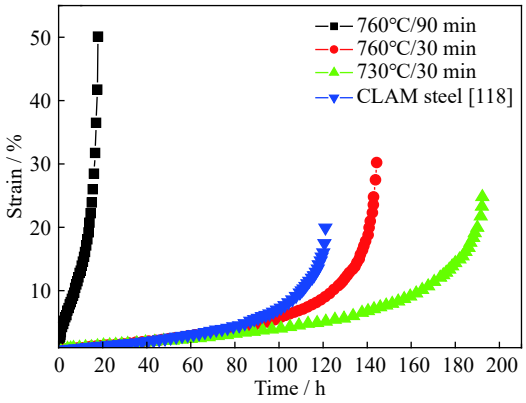

Fig. 12. Creep curves for the 0.10wt% Ti CLAM steels fabricated by different tempering processes at 600°C/170 MPa. The creep curve for the steel without Ti addition is also shown for comparison.

4. Summary

The main strengthening mechanisms of RAFM steels have been reviewed in detail. The high-temperature mechanical properties of RAFM steels can be significantly improved by optimizing the strengthening mechanisms. Compared with the creep life of the traditional RAFM steel, that of the 9Cr ODS steel is ~1000 times higher under 650°C/130 MPa, that of the SPD 9Cr2WVTa steel is ~30 times higher under 550°C/270 MPa, that of the TMT 9Cr–1W–0.06Ta steel is ~20 times higher under 550°C/260 MPa, and that of the tempered 0.10wt% Ti CLAM steel is ~1.5 times higher under 600°C/170 MPa. However, the preparation processes of the ODS steel and cold deformation and thermal deformation-strengthened RAFM steel are relatively complex, which limits their commercial production. Although the tempering process is simple, the increment of mechanical properties is lower compared with those of other processes. Some problems remain to be solved for the development of new RAFM steels. For example, whether or not the welding performance of the steel changes or not with the change in microstructure is still unclear. For the irradiation resistance of the RAFM steel, although the nano-sized precipitates effectively improve the irradiation resistance, the data of the microstructure and mechanical properties of the new steel under irradiation are still scarce. Except for the $M_{23}C_6$ carbide coarsening, the most important factors affecting the high-temperature stability of steels include grain boundary sliding and subgrain coarsening. Therefore, improving the grain boundary and subgrain boundary strengthening at high temperatures is important to develop high-performance RAFM steels.

Acknowledgements

This project is supported by the National Key Research and Development Program of China (No. 2016YFB 0300600), the National Natural Science Foundation of China (NSFC) (No. 51922026), the Fundamental Research Funds for the Central Universities (Nos. N2002013, N2002005, and N2007011), and the 111 Project (No. B20029).

References

[1] Q. Huang, N. Baluc, Y. Dai, S. Jitsukawa, A.Kimura, J. Konys, R.J. Kurtz, R. Lindau, T. Muroga, G.R. Odette, B. Raj, R.E. Stoller, L. Tan, H. Tanigawa, A.A.F. Tavassoli, T. Yamamoto, F. Wan, and Y. Wu, Recent progress of R&D activities on reduced activation ferritic/martensitic steels, *J. Nucl. Mater.*, 422(2013), No. 1-3, p. S2.

[2] K.C. Sahoo, J. Vanaja, P. Parameswaran, V.D. Vijayanand, and K. Laha, Effect of thermal ageing on microstructure, tensile and impact properties of reduced activated ferritic-martensitic steel, *Mater. Sci. Eng. A*, 686(2017), p. 54.

[3] C.L. Mao, C.X, Liu, L.M. Yu, H.J. Li, and Y.C. Liu, Mechanical properties and tensile deformation behavior of a reduced activated ferritic−martensitic (RAFM) steel at elevated temperatures, *Mater. Sci. Eng. A*, 725(2018), p. 283.

[4] T. Noda, F. Abe, H. Araki, and M. Okada, Materials selection for reduced activation of fusion reactors, *J. Nucl. Mater.*, 155-157(1988), p. 581.

[5] E.E. Bloom, R.W. Conn, J.W. Davis, R.E. Gold, R. Little, K.R. Schultz, D.L. Smith, and F.W. Wiffen, Low activation materials for fusion applications, *J. Nucl. Mater.*, 122(1984), No. 1-3, p. 17.

[6] R.L. Klueh, E.T. Cheng, M.L. Grossbeck, and E.E. Bloom, Impurity effects on reduced-activation ferritic steels developed for fusion applications, *J. Nucl. Mater.*, 280(2000), No. 3, p. 353.

[7] H. Tanigawa, Y. Someya, H. Sakasegawa, T. Hirose, and K. Ochiai, Radiological assessment of the limits and potential of reduced activation ferritic/martensitic steels, *Fusion Eng. Des.*, 89(2014), No. 7-8, p. 1573.

[8] R.L. Klueh and P.J. Maziasz, The microstructure of chromium−tungsten steels, *Metall. Trans. A*, 20(1989), No. 3, p. 373.

[9] R.L. Klueh, Heat treatment behavior and tensile properties of Cr−W steels, *Metall. Trans. A*, 20(1989), No. 3, p. 463.

[10] R.L. Klueh and W.R. Corwin, Impact behavior of Cr−W

steels, *J. Mater. Eng.*, 11(1989), No. 2, p. 169.
[11] S. Noh, M. Ando, H. Tanigawa, H. Fujii, and A. Kimura, Friction stir welding of F82H steel for fusion applications, *J. Nucl. Mater.*, 478(2016), p. 1.
[12] M. Kondo, M. Ishii, Y. Hishinuma, T. Tanaka, T. Nozawa, and T. Muroga, Metallurgical study on corrosion of RAFM steel JLF-1 in Pb−Li alloys with various Li concentrations, *Fusion Eng. Des.*, 125(2017), p. 316.
[13] K. Mukaia, F. Sanchezb, Chemical compatibility study between ceramic breeder and EUROFER97 steel for HCPB-DEMO blanket, *J. Nucl. Mater.*, 488(2017), p. 196.
[14] W.S. Tang, X.Q. Yang, S.L. Li, and H.J. Li, Microstructure and properties of CLAM/316L steel friction stir welded joints, *J. Mater. Process. Technol.*, 271(2019), p. 189.
[15] N.S. Shah, S. Sunil, and A. Sarkar, High temperature uniaxial compression and stress–relaxation behavior of India-specific RAFM steel, *Metall. Mater. Trans. A*, 49(2018), p. 2644.
[16] Y.B. Chun, S.H. Kang, S. Noh, T.K. Kim, D.W. Lee, S. Cho, and Y.H. Jeong, Effects of alloying elements and heat treatments on mechanical properties of Korean reduced-activation ferritic−martensitic steel, *J. Nucl. Mater.*, 455(2014), No. 1-3, p. 212.
[17] L. Tan, Y. Katoh, A.A.F. Tavassoli, J. Henry, M. Rieth, H. Sakasegawa, H. Tanigawa, and Q. Huang, Recent status and improvement of reduced-activation ferritic-martensitic steels for high-temperature service, *J. Nucl. Mater.*, 479(2016), p. 515.
[18] Y. Zhao, S. Liu, J. Shi, and X. Mao, Experimental and numerical simulation analysis on creep crack growth behavior of CLAM steel, *Mater. Sci. Eng. A*, 735(2018), p. 260.
[19] X. Hu, L.X. Huang, W. Yan, W. Wang, W. Sha, Y.Y. Shan, and K. Yang, Microstructure evolution in CLAM steel under low cycle fatigue, *Mater. Sci. Eng. A*, 607(2014), p. 356.
[20] P. Verma, N.C.S. Srinivas, S.R. Singh, and V. Singh, Low cycle fatigue behavior of modified 9Cr–1Mo steel at room temperature, *Mater. Sci. Eng. A*, 652(2016), p. 30.
[21] C. Zhang, L. Cui, Y.C. Liu, C.X. Liu, and H.J. Li, Microstructures and mechanical properties of friction stir welds on 9% Cr reduced activation ferritic/martensitic steel, *J. Mater. Sci. Technol.*, 34(2018), No. 5, p. 756.
[22] C. Zhang, L. Cui, D.P. Wang, Y.C. Liu, and H.J. Li, Effect of microstructures to tensile and impact properties of stir zone on 9%Cr reduced activation ferritic/martensitic steel friction stir welds, *Mater. Sci. Eng. A*, 729(2018), p. 257.
[23] S. Kumar, R. Awasthi, C.S. Viswanadham, K. Bhanumurthy, and G.K. Dey, Thermo-metallurgical and thermo-mechanical computations for laser welded joint in 9Cr–1Mo(V, Nb) ferritic/martensitic steel, *Mater. Des.*, 59(2014), p. 211.
[24] B. Arivazhagan, G. Srinivasan, S.K. Albert, and A.K. Bhaduri, A study on influence of heat input variation on microstructure of reduced activation ferritic martensitic steel weld metal produced by GTAW process, *Fusion Eng. Des.*, 86(2011), No. 2-3, p. 192.
[25] F.F. Luo, Z. Yao, L.P. Guo, J.P. Suo, and Y.M. Wen, Convoluted dislocation loops induced by helium irradiation in reduced-activation martensitic steel and their impact on mechanical properties, *Mater. Sci. Eng. A*, 607(2014), p. 390.
[26] C.C. Wang, C. Zhang, J.J. Zhao, Z.G. Yang, and W.B. Liu, Microstructure evolution and yield strength of CLAM steel in low irradiation condition, *Mater. Sci. Eng. A*, 682(2017), p. 563.
[27] W.H. Hu, L.P. Guo, J.H. Chen, F.F. Luo, T.C. Li, Y.Y. Ren, J.P. Suo, and F. Yang, Synergistic effect of helium and hydrogen for bubble swelling in reduced-activation ferritic/martensitic steel under sequential helium and hydrogen irradiation at different temperatures, *Fusion Eng. Des.*, 89(2014), No. 4, p. 324.
[28] D. Brimbal, L. Beck, O. Troeber, E. Gaganidze, P. Trocellier, J. Aktaa, and R. Lindau, Microstructural characterization of Eurofer-97 and Eurofer-ODS steels before and after multi-beam ion irradiations at JANNUS Saclay facility, *J. Nucl. Mater.*, 465(2015), p. 236.
[29] M. Dadé, J. Malaplate, J. Garnier, F.D. Geuser, F. Barcelo, P. Wident, and A. Deschamps, Influence of microstructural parameters on the mechanical properties of oxide dispersion strengthened Fe−14Cr steels, *Acta Mater.*, 127(2017), p. 165.
[30] S. Pal, M.E. Alam, S.A. Maloy, D.T. Hoelzer, and G.R. Odette, Texture evolution and microcracking mechanisms in as-extruded and cross-rolled conditions of a 14YWT nanostructured ferritic alloy, *Acta Mater.*, 152(2018), p. 338.
[31] Y. Zhang, C. Yu, T. Zhou, D.W. Liu, X.W. Fang, H.P. Li, and J.P. Suo, Effects of Ti and a twice-quenching treatment on the microstructure and ductile brittle transition temperature of 9CrWVTiN steels, *Mater. Des.*, 88(2015), p. 675.
[32] D. Wu, F.M. Wang, J. Cheng, and C.R. Li, Effect of Nb and V on the continuous cooling transformation of undercooled austenite in Cr–Mo–V steel for brake discs, *Int. J. Miner. Metall. Mater.*, 25(2018), No. 8, p. 892.
[33] Y. Li, P.F. Du, Z.H. Jiang, C.L. Yao, L. Bai, Q. Wang, G. Xu, C.Y. Chen, L. Zhang, and H.B. Li, Effects of TiC on the microstructure and formation of acicular ferrite in ferritic stainless steel, *Int. J. Miner. Metall. Mater.*, 26(2019), No. 11, p. 1385.
[34] J.G. Chen, C.X. Liu, Y.C. Liu, B.Y. Yan, and H.J. Li, Effects of tantalum content on the microstructure and mechanical properties of low-carbon RAFM steel, *J. Nucl. Mater.*, 479(2016), p. 295.
[35] X.W. Zhai, S.J. Liu, and Y.Y. Zhao, Effect of tantalum content on microstructure and tensile properties of CLAM steel, *Fusion Eng. Des.*, 104(2016), p. 21.
[36] J.H. Zhou, Y.F. Shen, Y.Y. Hong, W.Y. Xue, and R.D.K. Misra, Strengthening a fine-grained low activation martensitic steel by nanosized carbides, *Mater. Sci. Eng. A*, 769(2020), p. 138471.
[37] S.K. Albert, K. Lahaa, A.K. Bhaduria, T. Jayakumara, and E. Rajendrakumarb, Development of IN-RAFM steel and fabrication technologies for Indian TBM, *Fusion Eng. Des.*, 109-111(2016), p. 1422.
[38] J.B. Wang, Y.Y. Lian, F. Feng, Z. Chen, Y. Tan, S. Yang, X. Liu, J.B. Qiang, T.Z. Liu, M.Y. Wei, and Y.M. Wang, Microstructure of the tungsten and reduced activation ferritic−martensitic steel joint brazed with an Fe-based amorphous alloy, *Fusion Eng. Des.*, 138(2019), p. 164.
[39] C. Pandey, A. Giri, and M.M. Mahapatra, Evolution of phases in P91 steel in various heat treatment conditions and their effect on microstructure stability and mechanical properties, *Mater. Sci. Eng. A*, 664(2016), p. 58.
[40] S.H. Chen and L.J. Rong, Effect of silicon on the microstructure and mechanical properties of reduced activation ferritic/martensitic steel, *J. Nucl. Mater.*, 459(2015), p. 13.
[41] R. Agamennone, W. Blum, C. Gupta, and J.K. Chakravartty, Evolution of microstructure and deformation resistance in creep of tempered martensitic 9–12%Cr–2%W–5%Co steels, *Acta Mater.*, 54(2006), No. 11, p. 3003.
[42] B.Y. Yan, Y.C. Liu, Z.J. Wang, C.X. Liu, Y.H. Si, H.J. Li, and J.X. Yu, The effect of precipitate evolution on austenite grain

growth in RAFM steel, *Materials*, 10(2017), No. 9, p. 1017.
[43] H.K. Kim, J.W. Lee, J. Moon, C.H. Lee, and H.U. Hong, Effects of Ti and Ta addition on microstructure stability and tensile properties of reduced activation ferritic/martensitic steel for nuclear fusion reactors, *J. Nucl. Mater.*, 500(2018), p. 327.
[44] H.G. Tehrani-Moghadam, H.R. Jafarian, M.T. Salehi, and A.R. Eivani, Evolution of microstructure and mechanical properties of Fe–24Ni–0.3C TRIP steel during friction stir processing, *Mater. Sci. Eng. A*, 718(2018), p. 335.
[45] V. Sklenicka, J. Dvorak, P. Kral, Z. Stonawska, and M. Svoboda, Creep processes in pure aluminium processed by equal-channel angular pressing, *Mater. Sci. Eng. A*, 410-411(2005), p. 408.
[46] M.E. Kassner, The Effect of Low-Angle, and High-Angle Grain Boundaries on Elevated Temperature Strength, *MRS Proceedings*, 362(1994).
[47] Y. Jiao, L.J. Huang, S.L. Wei, H.X. Peng, Q. An, S. Jiang, and L. Geng, Constructing two-scale network microstructure with nano-Ti_5Si_3 for superhigh creep resistance, *J. Mater. Sci. Technol.*, 35(2019), No. 8, p. 1532.
[48] T. Takahashi, H. Nagai, and H. Oikawa, Effects of grain size on creep behaviour of Ti-50 mol.%Al intermetallic compound at 1100 K, *Mater. Sci. Eng. A*, 128(1990), No. 2, p. 195.
[49] S.G. Tian, B.S. Zhang, H.C. Yu, N. Tian, and Q.Y. Li, Microstructure evolution and creep behaviors of a directionally solidified nickel-base alloy under long-life service condition, *Mater. Sci. Eng. A*, 673(2016), p. 391.
[50] Y.B. Hu, L. Zhang. T.S. Cao, C.Q. Cheng, P.T. Zhao, G.P. Guo, and J. Zhao, The effect of thickness on the creep properties of a single-crystal nickel-based superalloy, *Mater. Sci. Eng. A*, 728(2018), p. 124.
[51] S.Y. Han, S.Y. Shin, C.H. Seo, H. Lee, J.H. Bae, K. Kim, S. Lee, and N.J. Kim, Effects of Mo, Cr, and V additions on tensile and charpy impact properties of API X80 pipeline steels, *Metall. Mater. Trans. A*, 40(2009), art. No. 1851.
[52] A.S. Taylor and P.D. Hodgson, Dynamic behavior of 304 stainless steel during high Z deformation, *Mater. Sci. Eng. A*, 528(2011), No. 9, p. 3310.
[53] G. Azevedo, R. Barbosa, E.V. Pereloma, and D.B. Santos, Development of an ultrafine grained ferrite in a low C–Mn and Nb–Ti microalloyed steels after warm torsion and intercritical annealing, *Mater. Sci. Eng. A*, 402(2005), No. 1-2, p. 98.
[54] A. Momeni and K. Dehghani, Hot working behavior of 2205 austenite–ferrite duplex stainless steel characterized by constitutive equations and processing maps, *Mater. Sci. Eng. A*, 528(2011), No. 3, p. 1448.
[55] M.E. Kassner, Recent developments in understanding the mechanism of five-power-law creep, *Mater. Sci. Eng. A*, 410-411(2005), p. 20.
[56] Y. Tsukada, A. Shiraki, Y. Murata, S. Takaya, T. Koyama, and M. Morinaga, Precipitation of ferromagnetic phase induced by defect energies during creep deformation in Type 304 austenitic steel, *J. Nucl. Mater.*, 401(2010), No. 1-3, p. 13.
[57] B.A. Szajewski, S.S. Chakravarthy, and W.A. Curtin, Operation of a 3D Frank–Read source in a stress gradient and implications for size-dependent plasticity, *Acta Mater.*, 61(2013), No. 5, p. 1469.
[58] G.A. Malygin, Mechanism of the formation of deformation steps of nanometric sizes at the surface of plastically deformed crystals, *Phys. Solid State*, 43(2001), p. 257.
[59] S.G. Tian, J.H. Yang, and X.F. Yu, Deformation features of AZ31 Mg-alloy in initial period of high temperature creep, *Acta Metall. Sin.*, 41(2005), No. 4, p. 375.
[60] Y. Li, Y.F. Li, B. Xu, Q.L. Li, G.G. Shu, and W. Liu, Magnetic properties of thermally aged Fe–Cu alloys with pre-deformation, *J. Iron. Steel Res. Int.*, 23(2016), No. 9, p. 981.
[61] A. Kostka, K.G. Tak, and G. Eggeler, On the effect of equal-channel angular pressing on creep of tempered martensite ferritic steels, *Mater. Sci. Eng. A*, 481-482(2008), p. 723.
[62] W. Liu, Y.H. Jiang, H. Guo, Y. Zhang, A.M. Zhao, and Y. Huang, Mechanical properties and wear resistance of ultrafine bainitic steel under low austempering temperature, *Int. J. Miner. Metall. Mater.*, 27(2020), No. 6, p. 483.
[63] K. Lu, Making strong nanomaterials ductile with gradients, *Science*, 345(2014), No. 6230, p. 1455.
[64] M. Taneike, F. Abe, and K. Sawada, Creep-strengthening of steel at high temperatures using nano-sized carbonitride dispersions, *Nature*, 424(2003), p. 294.
[65] L. Tan, L.L. Snead, and Y. Katoh, Development of new generation reduced activation ferritic–martensitic steels for advanced fusion reactors, *J. Nucl. Mater.*, 478(2016), p. 42.
[66] T.P. Hou and K.M. Wu, Alloy carbide precipitation in tempered 2.25 Cr–Mo steel under high magnetic field, *Acta Mater.*, 61(2013), No. 6, p. 2016.
[67] J.R. Croteau, S. Griffiths, M.D. Rossell, C. Leinenbach, C. Kenel, V. Jansena, D.N. Seidmana, D.C. Dunanda, and N.Q. Voa, Microstructure and mechanical properties of Al–Mg–Zr alloys processed by selective laser melting, *Acta Mater.*, 153(2018), p. 35.
[68] L. Sun, T.H. Simm, T.L. Martin, S. Mcadam, D.R. Galvin, K.M. Perkins, P.A.J. Bagot, M.P. Moody, S.W. Ooi, P. Hill, M.J. Rawson, and H.K.D.H. Bhadeshia, A novel ultra-high strength maraging steel with balanced ductility and creep resistance achieved by nanoscale β-NiAl and Laves phase precipitates, *Acta Mater.*, 149(2018), p. 285.
[69] H. Tanaka, M. Murata, F. Abe, and K. Yagi, The effect of carbide distributions on long-term creep rupture strength of SUS321H and SUS347H stainless steels, *Mater. Sci. Eng. A*, 234-236(1997), p. 1049.
[70] A. Baltušnikas, I. Lukošiūtė, V. Makarevičius, R. Kriūkienė, and A. Grybėnas, Influence of thermal exposure on structural changes of $M_{23}C_6$ carbide in P91 steel, *J. Mater. Eng. Perform.*, 25(2016), p. 1945.
[71] W.Y. Xue, J.H. Zhou, Y.F. Shen, W.N. Zhang, and Z.Y. Liu, Micromechanical behavior of a fine-grained CLAM steel, *J. Mater. Sci. Technol.*, 35(2019), No. 9, p. 1869.
[72] K.S. Cho, S.S. Park, D.H. Choi, and H. Kwon, Influence of Ti addition on the microstructure and mechanical properties of a 5% Cr–Mo–V steel, *J. Alloys Compd.*, 626(2015), p. 314.
[73] M. Tamura, K. Shinozuka, K. Masamura, K. Ishizawa, and S. Sugimoto, Solubility product and precipitation of TaC in Fe–8Cr–2W steel, *J. Nucl. Mater.*, 258-263(1998), p. 1158.
[74] G.E. Lucas, The evolution of mechanical property change in irradiated austenitic stainless steels, *J. Nucl. Mater.*, 206(1993), No. 2-3, p. 287.
[75] C.S. Wang, Y.A. Guo, J.T. Guo, and L.Z. Zhou, Microstructural characteristics and mechanical properties of a Mo modified Ni–Fe–Cr based alloy, *Mater. Sci. Eng. A*, 675(2016), p. 314.
[76] X. Yang, B. Liao, F.R. Xiao, W. Yan, Y.Y. Shan, and K. Yang, Ripening behavior of $M_{23}C_6$ carbides in P92 steel during aging at 800°C, *J. Iron Steel Res. Int.*, 24(2016), No. 8, p. 858.
[77] Z.F. Peng, S. Liu, C. Yang, F.Y. Chen, and F.F. Peng, The effect of phase parameter variation on hardness of P91 compon-

ents after service exposures at 530–550°C, *Acta Mater.*, 143(2018), p. 141.
[78] Y.P. Zeng, J.D. Jia, W.H. Cai, S.Q. Dong, and Z.C. Wang, Effect of long-term service on the precipitates in P92 steel, *Int. J. Miner. Metall. Mater.*, 25(2018), No. 8, p. 913.
[79] C.C. Zhao, Y.F. Zhou, X.L. Xing, S. Liu, X.J. Ren, and Q.X. Yang, Precipitation stability and micro-property of (Nb, Ti)C carbides in MMC coating, *J. Alloys Compd.*, 763(2018), p. 670.
[80] W. Yan, W. Wang, Y.Y. Shan, and K. Yang, Microstructural stability of 9–12%Cr ferrite/martensite heat-resistant steels, *Front. Mater. Sci.*, 7(2013), No. 1, p. 1.
[81] K. Sawada, K. Kubo, and F. Abe, Contribution of coarsening of MX carbonitrides to creep strength degradation in high chromium ferritic steel, *Mater. Sci. Technol.*, 19(2003), No. 6, p. 732.
[82] X.S. Zhou, C.X. Liu, L.M. Yu, Y.C. Liu, and H.J. Li, Phase transformation behavior and microstructural control of high-Cr martensitic/ferritic heat-resistant steels for power and nuclear plants: A review, *J. Mater. Sci. Technol.*, 31(2015), No. 3, p. 235.
[83] C. Liu, Q.Q. Shi, W. Yan, C.G. Shen, K. Yang, Y.Y. Shan, and M.C. Zhao, Designing a high Si reduced activation ferritic/martensitic steel for nuclear power generation by using Calphad method, *J. Mater. Sci. Technol.*, 35(2019), No. 3, p. 266.
[84] C.M. Barr, P.J. Felfer, J.I. Cole, and M.L. Taheri, Observation of oscillatory radiation induced segregation profiles at grain boundaries in neutron irradiated 316 stainless steel using atom probe tomography, *J. Nucl. Mater.*, 504(2018), p. 181.
[85] S. Ishino, N. Sekimura, K. Murakami, and H. Abe, Some remarks on in-situ studies using TEM-heavy-ion accelerator link from the stand point of extracting radiation damage caused by fast neutrons, *J. Nucl. Mater.*, 471(2016), p. 167.
[86] F.D. Chen, X.B. Tang, Y.H. Yang, H. Huang, J. Liu, H. Li, and D. Chen, Atomic simulations of Fe/Ni multilayer nanocomposites on the radiation damage resistance, *J. Nucl. Mater.*, 468(2016), p. 164.
[87] P.P. Liu, M.Z. Zhao, Y.M. Zhu, J.W. Bai, F.R. Wan, and Q. Zhan, Effects of carbide precipitate on the mechanical properties and irradiation behavior of the low activation martensitic steel, *J. Alloys Compd.*, 579(2013), p. 599.
[88] X. Wang, Q.Z. Yan, G.S. Was, and L.M. Wang, Void swelling in ferritic-martensitic steels under high dose ion irradiation: Exploring possible contributions to swelling resistance, *Scripta Mater.*, 112(2016), p. 9.
[89] G.A. Vetterick, J. Gruber, P.K. Suri, J.K. Baldwin, M.A. Kirk, P. Baldo, Y.Q. Wang, A. Misra, G.J. Tucker, and M.L. Taheri, Achieving radiation tolerance through non-equilibrium grain boundary structures, *Sci. Rep.*, 7(2017), art. No. 12275.
[90] S.F.Li, Z.J. Zhou, J.S. Jang, M. Wang, H.L. Hu, H.Y. Sun, L. Zou, G.M. Zhang, and L.W. Zhang, The influence of Cr content on the mechanical properties of ODS ferritic steels, *J. Nucl. Mater.*, 455(2014), No. 1-3, p. 194.
[91] C. Pandey, M.M. Mahapatra, P. Kumar, R.S. Vidyrathy, and A. Srivastava, Microstructure-based assessment of creep rupture behaviour of cast-forged P91 steel, *Mater. Sci. Eng. A*, 695(2017), p. 291.
[92] T. Yamashiro, S. Ukai, N. Oono, S. Ohtsuka, and T. Kaito, Microstructural stability of 11Cr ODS steel, *J. Nucl. Mater.*, 472(2016), p. 247.
[93] J.J. Huet, Possible fast-reactor canning material strengthened and stabilized by dispersion, *Powder Metall.*, 10(1967), No. 20, p. 208.
[94] C.A. Williams, P. Unifantowicz, N. Baluc, G.D.W. Smith, and E.A. Marquis, The formation and evolution of oxide particles in oxide-dispersion-strengthened ferritic steels during processing, *Acta Mater.*, 61(2013), No. 6, p. 2219.
[95] R.L. Klueh, P.J. Maziasz, I.S. Kim, L. Heatherly, D.T. Hoelzer, N. Hashimoto, E.A. Kenik, and K. Miyahara, Tensile and creep properties of an oxide dispersion-strengthened ferritic steel, *J. Nucl. Mater.*, 307-311(2002), p. 773.
[96] P. Dou, A. Kimura, T. Okuda, M. Inoue, S. Ukai, S. Ohnuki, T. Fujisawa, and F. Abe, Polymorphic and coherency transition of Y–Al complex oxide particles with extrusion temperature in an Al-alloyed high-Cr oxide dispersion strengthened ferritic steel, *Acta Mater.*, 59(2011), No. 3, p. 992.
[97] G.M. Zhang, Z.J. Zhou, K. Mo, P.H. Wang, Y.B. Miao, S.F. Li, M. Wang, X. Liu, M.Q. Gong, J. Almer, and J.F. Stubbins, The microstructure and mechanical properties of Al-containing 9Cr ODS ferritic alloy, *J. Alloys Compd.*, 648(2015), p. 223.
[98] P. Dou, A. Kimura, R. Kasada, T. Okuda, M. Inoue, S. Ukai, S. Ohnuki, T. Fujisawa, and F. Abe, TEM and HRTEM study of oxide particles in an Al-alloyed high-Cr oxide dispersion strengthened steel with Zr addition, *J. Nucl. Mater.*, 444(2014), No. 1-3, p. 441.
[99] P.Y. Yan, L.M. Yu, Y.C. Liu, C.X. Liu, H.J. Li, and J.F. Wu, Effects of Hf addition on the thermal stability of 16Cr–ODS steels at elevated aging temperatures, *J. Alloys Compd.*, 739(2018), p. 368.
[100] S.J. Zinkle, J.L. Boutard, D.T. Hoelzer, A. Kimura, R. Lindau, G.R. Odette, M. Rieth, L. Tan, and H. Tanigawa, Development of next generation tempered and ODS reduced activation ferritic/martensitic steels for fusion energy applications, *Nucl. Fusion*, 57(2017), No. 9, art. No. 092055.
[101] S. Xu, L.Z. Chen, S.G. Cao, H.D. Jia, and Z.J. Zhou, Research progress on microstructure design and control of ODS steels application for advanced nuclear energy systems, *Mater. Rep.*, 33(2019), No. 1, p. 78.
[102] H.S. Legagneur, S. Vincent, J. Garnier, A.F. Gourgues-Lorenzon, and E. Andrieu, Anisotropic intergranular damage development and fracture in a 14Cr ferritic ODS steel under high-temperature tension and creep, *Mater. Sci. Eng. A*, 722(2018), p. 231.
[103] C. Dethloff, E. Gaganidze, and J. Aktaa, Quantitative TEM analysis of precipitation and grain boundary segregation in neutron irradiated EUROFER97, *J. Nucl. Mater.*, 454(2014), No. 1-3, p. 323.
[104] T. Jaumier, S. Vincent, L. Vincent, and R. Desmorat, Creep and damage anisotropies of 9%Cr and 14%Cr ODS steel cladding, *J. Nucl. Mater.*, 518(2019), p. 274.
[105] D. Kumar, U. Prakash, V.V. Dabhade, K. Laha, and T. Sakthivel, Development of oxide dispersion strengthened (ODS) ferritic steel through powder forging, *J. Mater. Eng. Perform.*, 26(2017), p. 1817.
[106] P. Wang, T.H. Yin, and S.X. Qu, On the grain size dependent working hardening behaviors of severe plastic deformation processed metals, *Scripta Mater.*, 178(2020), p. 171.
[107] Z.J. Yang, K.K. Wang, and Y. Yang, Optimization of ECAP–RAP process for preparing semisolid billet of 6061 aluminum alloy, *Int. J. Miner. Metall. Mater.*, 27(2020), p. 792.
[108] L.M. Wang, Z.B. Wang, and K. Lu, Grain size effects on the austenitization process in a nanostructured ferritic steel, *Acta Mater.*, 59(2011), No. 9, p. 3710.
[109] S.H. Chen, X.J. Jin, and L.J. Rong, Improving the strength and

ductility of reduced activation ferritic/martensitic steel by cold-swaging and post-annealing, *Mater. Sci. Eng. A*, 631(2015), p. 139.

[110] X.J. Jin, S.H. Chen, and L.J. Rong, Microstructure modification and mechanical property improvement of reduced activation ferritic/martensitic steel by severe plastic deformation, *Mater. Sci. Eng. A*, 712(2018), p. 97.

[111] J. Hoffmann, M. Rieth, L. Commin, P. Fernández, and M. Roldánb, Improvement of reduced activation 9%Cr steels by ausforming, *Nucl. Mater. Energy*, 6(2016), p. 12.

[112] X. Xiao, G.Q. Liu, B.F. Hu, J.S. Wang, and A. Ullah, Effect of V and Ta on the precipitation behavior of 12%Cr reduced activation ferrite/martensite steel, *Mater. Charact.*, 82(2013), p. 130.

[113] W.T. Huo, J.T. Shi, L.G. Hou, and J.S. Zhang, An improved thermo-mechanical treatment of high-strength Al–Zn–Mg–Cu alloy for effective grain refinement and ductility modification, *J. Mater. Process. Technol.*, 239(2017), p. 303.

[114] R.L. Klueh, N. Hashimoto, and P.J. Maziasz, New nano-particle-strengthened ferritic/martensitic steels by conventional thermo-mechanical treatment, *J. Nucl. Mater.*, 367–370(2007), p. 48.

[115] P. Prakash, J. Vanaja, N. Srinivasan, P. Parameswaran, G.V.S. Nageswara Rao, and K. Laha, Effect of thermo-mechanical treatment on tensile properties of reduced activation ferritic-martensitic steel, *Mater. Sci. Eng. A*, 724(2018), p. 171.

[116] X. Xiao, G.Q. Liu,B.F. Hu, J.S. Wang, and W.B. Ma, Microstructure stability of V and Ta microalloyed 12% Cr reduced activation ferrite/martensite steel during long-term aging at 650°C, *J. Mater. Sci. Technol.*, 31(2015), No. 3, p. 311.

[117] L.X. Huang, *Study on Evolution of Microstructure and Mechanical Properties Atelevated Temperature for CLAM Steel* [Dissertation], Yanshan University, Qinghuangdao, 2014.

[118] B.Y. Zhong, B. Huang, C.J. Li, S.J. Liu, G. Xu, Y.Y. Zhao, and Q.Y. Huang, Creep deformation and rupture behavior of CLAM steel at 823 K and 873 K, *J. Nucl. Mater.*, 455(2014), No. 1-3, p. 640.